Received: 22 December 2023 | Accepted: 27 March 2024

DOI: 10.1002/vzj2.20339

Vadose Zone Journal

TECHNICAL NOTE

Special Section: Tribute to Rien van Genuchten, Recipient of the 2023 Wolf Prize for Agriculture

Simulating bare soil evaporation for undisturbed soil cores—Using HYDRUS 3D simulation on X-ray µCT determined soil macrostructures

Frederic Leuther | **Efstathios Diamantopoulos**

Chair of Soil Physics, University of Bayreuth, Bayreuth, Germany

Correspondence
Frederic Leuther, Chair of Soil Physics, University of Bayreuth, Universitätsstr. 30, 95447, Bayreuth, Germany.
Email: frederic.leuther@uni-bayreuth.de

Assigned to Associate Editor Jan Hopmans.

Funding information
Open Access Publishing Fund of the University of Bayreuth

Abstract

Evaporation of soil water depends not only on climatic conditions, soil surface roughness, soil texture, and soil hydraulic properties but also on the soils' macrostructure. Evaporation is characterized by water losses over time for a defined soil volume, where soils are assumed to be homogeneous in texture and structure. In this technical note, we investigated the potential and limitations of 3D modeling of evaporation processes on 250 cm^3 soil cores with structural features ≥480 µm determined by X-ray computed tomography. For this, we used isothermal Richards equation as the main governing equation, accounting also for isothermal vapor flow. We simulated two evaporation experiments with same soil texture but contrasting macrostructures, that is, the spatial arrangement of voxels classified as soil matrix and air-filled voids, of a ploughed and non-ploughed grassland soil with HYDRUS 3D. In both simulations, we fixed the potential evaporation rates to the experimental rates and evaluated simulation results with measured matric potential data at two depths (1.25 cm and 3.75 cm) continuously recorded at 10 min intervals. We could show that the simulations of bare soil evaporation were able to predict the tensiometer dynamics and water losses for the full experimental time of 7 days. The simulation provided unique spatial information of water content and flow velocities as a function of time, which are important when studying the effect of air-filled macropores, macro-connectivity of soil matrix, and water dynamics on soil evaporation.

1 | INTRODUCTION

Bare soil evaporation, a fundamental component of the Earth's hydrological cycle (Allen, 1998; Bittelli et al., 2008), refers to the process by which water is converted from a liquid state to vapor state and includes liquid water flow, vapor and energy flow, and phase change (Vanderborght et al., 2017). Depending on soil wetness, it is controlled by convective and diffusive water fluxes near the soil surface, as well as the hydraulic and structural properties of the uppermost soil layer (Brutsaert & Chen, 1995; Or et al., 2013; Philip & Vries, 1957). To satisfy the atmospheric demand on the soil surface, water must be transported from deeper soil to the surface by capillarity or through the soil matrix via vapor diffusion (Geistlinger & Leuther, 2018). Since unsaturated hydraulic conductivity in soils decreases with decreasing water

Abbreviations: PDI, Peters–Durner–Ideen; SHP, soil hydraulic properties; X-ray µCT, X-ray computed tomography.

content, diffusion becomes the dominant effect when the surface becomes dry, which continuously reduces the evaporation rate (Iden, Diamantopoulos et al., 2021; Or et al., 2013).

Soil structure, defined as the three-dimensional (3D) arrangement of solids and pores, affects soil evaporation through different processes. The soil surface and its roughness define the interfacial area between soil and atmosphere, the structure of the boundary layer, and thus evaporation rate for given driving climatic forces. Porosity, pore size distribution, and the connectivity of the pore network determines how much water is stored in the soil and how fast water can be transported toward the evaporating soil surface (Prat, 2007, 2011). Here, soil texture is an important determinant. Although the effect of pore-scale processes on bare soil evaporation have been extensively tested, the opposite is observed for larger scale processes. For example, at the mm to cm scale and when soils are unsaturated, the arrangement of air-filled pores, soil clods, and rocks becomes an important determinant, which affect water flow through non-permeable areas (stones and air-filled pores) or bottlenecks due to limited contact points between clods. In this technical note, we define macrostructure as the spatial arrangement of voxels classified as soil matrix and air-filled voids ≥0.48 mm measured by X-ray computed tomography (X-ray μCT). Integrating the different processes that determine soil evaporation is a key to quantifying water losses from soils under various climatic conditions and land management practices.

Simulating water flow under bare soil evaporation requires coupled flow of liquid water, water vapor, and energy, and the theory was described by Philip and De Vries (1957) and was later extended by other researchers (Milly, 1984; Nassar & Horton, 1997; Vanderborght et al., 2017). The theory has successfully been tested against experimental observations (Sakai et al., 2011). Very recently, Iden, Blöcher et al. (2021) showed that for typical laboratory evaporation experiments, an isothermal flow model can accurately simulate bare soil evaporation experiments, but only if an isothermal vapor diffusion model is added to the hydraulic conductivity curve (Peters, 2013). HYDRUS 3D enables us to simulate water flow on 3D domains of general geometry under well-defined boundary conditions using the Richards equation as the main equation. We note that Richards equation is a continuum equation that requires the definition of macroscopic soil hydraulic properties (SHP) defined at the representative elementary volume (REV) scale, meaning that we cannot study pore scale processes with it. However, we can use Richards equation to estimate the effect of air-filled macro-porosity on the overall unsaturated water flow in soil.

In this technical note, we present a method to study the evaporation process of soil cores based on X-ray μCT imaging and HYDRUS 3D simulation of water flow. Therefore, we simulated two evaporation experiments of soil cores with contrasting macrostructures (ploughed and non-ploughed grassland soils) but same texture and organic matter content. Since the focus was on the effect of macrostructure on bare soil evaporation dynamics, we simulated isothermal liquid and vapor flow of 3D real soil systems by importing the complex geometry into Hydrus 3D based on X-ray μCT images. For both macrostructures, we used initial water content and weight changes determined in an evaporation experiment as boundary conditions, and water potential measurements in 1.25-cm and 3.75-cm depth for evaluation. Water distributions and flow velocity within the samples were used as indicators to evaluate the spatial heterogeneity in water flow during bare soil evaporation caused by soil macrostructure.

Core Ideas

- The authors present a methodology to conduct 3D simulations with HYDRUS Suite for real soil systems based on X-ray μCT images.
- The authors present 3D simulation of bare soil evaporation on structured soils.
- The authors evaluate the simulations using mass loss and tensiometer measurements.
- The authors present quantification and visualization of the effects of soil structure on soil water dynamics.

2 | MATERIALS AND METHODS

2.1 | Soil samples, evaporation experiments, and hydraulic properties

This study is based on soil cores taken in Giessen, Germany, with a silt clay texture of 20% sand, 40% silt, 40% clay (DIN), and an organic matter content of 4.46% (Jäger et al., 2003). First, undisturbed soil cores with a volume of 250 cm^3 were taken below the grass cover at a depth of 5–10 cm. The mean bulk density was 1.06 g cm^{-3}. Second, soil clods (0.5–3.5 cm) were collected from a ploughed soil in the vicinity and packed in 250 cm^3 cylinders to a bulk density of 0.70 g cm^{-3} to simulate the loose packing at the very surface of a ploughed field (Daraghmeh et al., 2009). Soil information and X-ray μCT imaging for all samples are described in detail in Leuther and Schlüter (2021).

For this technical note, experimental results for one undisturbed soil column (grassland) and one column representing a ploughed field were selected (ploughed). Both samples were saturated for 24 h with tap water and drained on a sandbox to −10 hPa to exclude the biggest pores ($r \geq 150$ μm) from the evaporation experiment. For both samples, evaporation

TABLE 1 Soil hydraulic properties, boundary condition, and initial condition of the tested soil columns as implemented in HYDRUS 3D. Soil hydraulic properties were described using a bimodal Peters–Durner–Iden (PDI) model.

		Initial condition		
	Boundary condition	Hydrostatic distribution of h		Domain
Land use	Surface area (cm^2)	Bottom pressure head (cm)	Top pressure head (cm)	Total water volume (cm^3)
Grassland	61	1.25	−3.75	124
Ploughed	83	−14.0	−19.0	67
Grassland: Soil hydraulic properties for the bimodal-PDI model				
θ_r (cm^3 cm^{-3})	θ_s (cm^3 cm^{-3})	α_1/α_2 (cm^{-1})	n_1/n_2 (−)	w_2
0.183	0.575	0.0041/0.1005	3.422/1.049	0.918
K_s (cm day^{-1})	τ (−)	ω (−)	α_{film} (−)	pF_0
1045	6.1	1.10×10^{-4}	−1.5	6.8
Ploughed: Soil hydraulic properties for the bimodal-PDI model				
θ_r (cm^3 cm^{-3})	θ_s (cm^3 cm^{-3})	α_1/α_2 (cm^{-1})	n_1/n_2 (−)	w_2
0.219	0.462	0.0085/0.0217	1.01/1.86	0.075
K_s (cm day^{-1})	τ (−)	ω (−)	α_{film} (−)	pF_0
10	7.0	1.13×10^{-6}	−1.5	6.8

experiments were conducted using the HYPROP device (METER Group). During the experiments, the cumulative evaporation was continuously monitored with an electronic balance as well as the matric potential at two different depths: $z_1 = 1.25$ cm and $z_2 = 3.75$ cm from the bottom of the soil cores. The SHP, that is, the soil water retention curve and unsaturated hydraulic conductivity, were also determined using the evaporation method (Schindler, 1980) as implemented in the HYPROP-fit software (LABROS Soil View V5.1.0.0). A bimodal Peters–Durner–Iden (PDI) model (Peters, 2013; Weber et al., 2017) was fitted to the experimental SHP to characterize the hydraulic properties from saturation to very dry conditions (Table 1).

2.2 | X-ray µCT imaging and processing

Leuther and Schlueter (2021) scanned all samples with an industrial X-ray µCT device (X-Tek Systems Ltd.; XT H 225; Nikon Metrology). The samples were scanned for 47 min using a 0.7-mm copper filter at 150 kV, 310 µA, resulting in 2000 projections (0.708 s per projections). A voxel resolution of 48 µm was achieved at an 8-bit grayscale resolution in the reconstructed tomogram (Figure 1a).

Image processing and analysis were done with the open-source software package Fiji ImageJ v1.53 (Schindelin et al., 2012). First, the images were filtered with a two-dimensional (2D) non-local means filter (Buades et al., 2011) to reduce image noise. Second, filtered images were corrected for vertical differences in average image intensity due to shading and cone beam artifacts (Schlüter et al., 2016). Third, images were segmented into air-filled pore space and soil matrix by using the fuzzy c-means thresholding method (Jawahar et al., 1997). Forth, the area outside the soil core (cylinder and air) was also labeled as air. As a result, the binary image contained the information soil matrix and air, and the spatial arrangement of the soil matrix voxels defined the macrostructure to be used for simulation.

2.3 | HYDRUS 3D modeling of soil water evaporation for real geometry

HYDRUS 3D is limited to the number of nodes that can be used for the simulation domain, and for this reason, we scaled the segmented images by factor 0.1 to a voxel resolution of 480 µm. By doing so, we could simulate evaporation on the full sample size of 250 cm^3 but we also reduced information density on structural heterogeneity. The scaling created some isolated voxels at the surface, which were removed by connected component labeling implemented in the MorphoLibJ-Plugin (Legland et al., 2016) to avoid numerical problems in the simulation.

In HYDRUS (Šimůnek et al., 2018), a cuboid domain was initially created with the following dimensions: 7.6 × 7.6 × 5 cm, and it was further divided into three numerical layers:

1. Layer 1: From the top of the column to 1.5-cm depth.
2. Layer 2: From 1.5-cm depth to 2.5-cm depth.
3. Layer 3: From 2.5 cm to the bottom of the cuboid (5 cm).

For all three numerical layers, an element size of 0.05 cm (Layer 1), 0.10 cm (Layer 2), and 0.20 cm (Layer 3) was

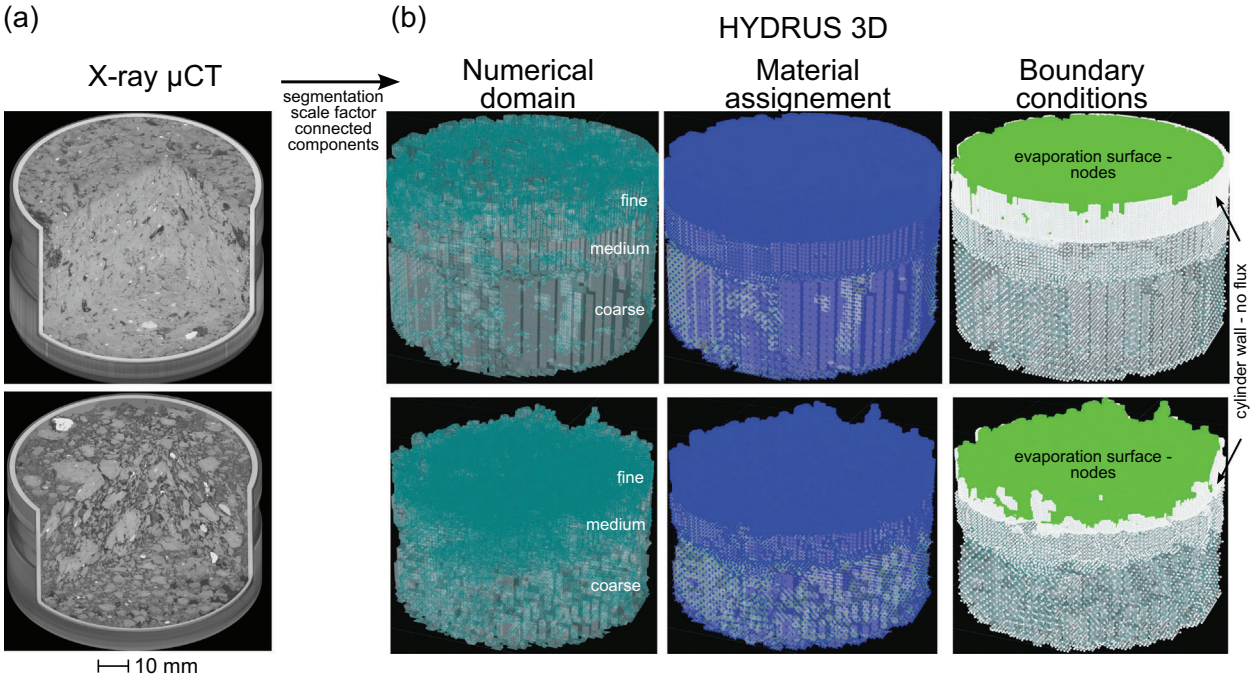

FIGURE 1 (a) Filtered X-ray computed tomography (X-ray µCT) tomograms of the grassland (top) and ploughed soil (bottom) scanned at a voxel resolution of 48 µm. Black objects display air-filled pores and gray represents solid soil matrix. (b) HYDRUS 3D: Numerical domain (turquoise) with three different layers in element sizes, material assignment (blue represents soil, transparent represents air), and evaporation surface (green) as boundary condition of the segmented and scaled images with a voxel resolution of 480 µm.

selected, respectively, and the numerical mesh was created. In that way, we achieved a higher number of numerical nodes and elements near the soil surface, where higher gradients of matric potential are expected (Figure 1b). The total number of numerical nodes varied between around 480,000 nodes for the grassland column and 400,000 for the ploughed column. This corresponds to a total number of 3D elements between 530,000 and 820,000, respectively. The difference is attributed to the less total soil volume for the ploughed soil columns, especially near the top of the column, and the higher discretization for Layer 1. Elements, which were classified as air space during image processing, were deleted and only the soil matrix elements remained. Finally, isolated elements, if any, were further removed from the domain by visual inspection.

The next step was to assign local SHP to all the numerical nodes. First, we modified the fitted PDI models by adding an isothermal vapor conductivity component to the unsaturated hydraulic conductivity curve, which defines molecular diffusion of water vapor in soil (Iden, Blöcher et al., 2021). We assumed a constant temperature of 20°C since evaporation experiments were conducted under laboratory condition. This process is important for simulating isothermal bare soil evaporation (Iden, Blöcher et al., 2021; Iden, Diamantopoulos et al., 2021). Second, we assigned the same local SHP for all the numerical nodes based on the PDI functions described above. This means that the PDI functions fitted to the experimental SHPs for the grassland column (Table 1) were corrected for isothermal vapor conductivity and assigned to all the numerical nodes of the grassland column simulation. Similarly, the corrected PDI model for the ploughed soil column was assigned to all the numerical nodes of the column simulation.

For the grassland column, we assumed a hydrostatic initial distribution of the pressure head with $h_{\text{init}}^{\text{grassland}}(x, y, z = 0, t = 0) = +1.25$ cm and $h_{\text{init}}^{\text{grassland}}(x, y, z = 5, t = 0) = -3.75$ cm, respectively ($z = 0$ at the bottom of the soil column). This value distribution was assumed according to the tensiometer readings. Similarly, for the ploughed soil, we assumed $h_{\text{init}}^{\text{ploughed}}(x, y, z = 0, t = 0) = -13.9$ cm and $h_{\text{init}}^{\text{ploughed}}(x, y, z = 5, t = 0) = -18.9$ cm as measured by the tensiometers. Initially, for all the numerical nodes, a no-flow boundary condition (white nodes in Figure 1b) was assigned. Afterward, all the nodes of Layer 1 have been selected, and an evaporation boundary condition has been assigned. However, to avoid evaporation from the sides of the domain, where after sampling, soil was in direct contact with the metallic cylinder, a 2D view (x-y from top) of the column was created, and all the nodes outside a circle with a diameter of 7.4 cm were converted back to no flow nodes. In that way, evaporation was restricted to the surface nodes of Layer 1 down to 1.5-cm depth. For all the selected evaporation nodes (green nodes in Figure 1b), a two-type boundary condition is assumed in HYDRUS 3D. First, for each column, a

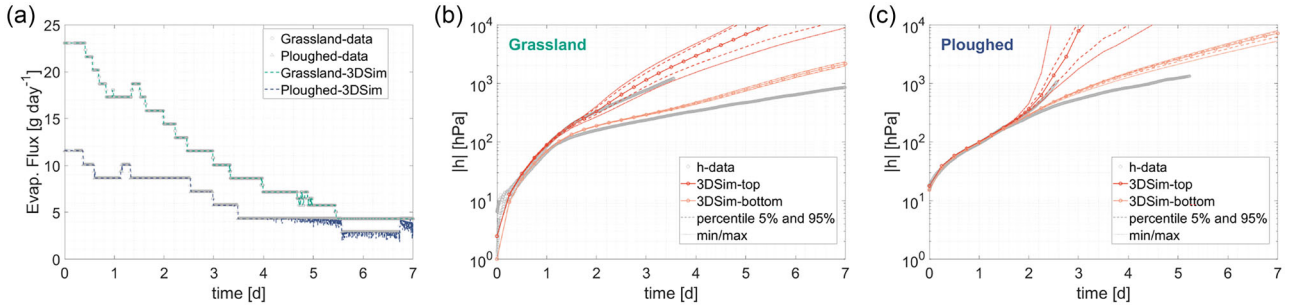

FIGURE 2 (a) Evaporation rate for both columns measured during the experiments (circles) and simulated data (dashed lines), measured and simulated potential in the grassland column (b) and the ploughed soil (c) in 1.25 cm (top) and 3.75 cm (bottom) depth.

time series of evaporation rate (cm day^{-1}) was calculated from the Hyprop balance data. Afterwards, this rate time series was applied as a potential evaporation rate. The critical pressure head h_{crit}, which describes in HYDRUS the change of the boundary condition from a Neumann type (flux type) to a Dirichlet type (constant head type), was set equal to -6.2×10^6 cm (pF 6.79), which corresponds to very dry condition at a water content of 0.001 cm^3 cm^{-3}. The simulations were executed for a simulation time of 7 days, and visualization of water contents and fluxes was done by using ParaView (Hansen & Johnson, 2005).

3 | RESULTS

HYDRUS 3D simulated the full range of actual evaporation fluxes determined by the weight loss during the laboratory experiment (Figure 2a). For the ploughed soil experiment, numerical fluctuations in water loss were determined after 4 days, but these had no effect on the cumulative water loss (Figure S1). The ploughed soil had a constant water loss of about 10 g water per day for 2.5 days, thereafter, it decreased for 1 day to 5 g water per day. For the grassland soil, the evaporation flux decreased continuously from 18 to 5 g water per day after 1.75 days. In both experiments, the simulated water potentials at a depth of 1.25 cm were within the range of the measured potential (Figure 2b,c). For the ploughed soil, the exponential increase in the water potential and the wide range of simulated potentials after 2.5 days indicated rapid drying and great spatial heterogeneity in the uppermost soil layers (Figure 2c). For both soils, the potentials measured in the lower part of the soil cores (3.75-cm depth) were well described at the beginning of the experiments but were systematically underestimated by the simulation during drying, <−200 hPa for grassland (Figure 2b) and <−400 hPa for ploughed soil (Figure 2c). Overall, both the slope and the magnitude of the potentials, which were recorded as point measurements, were reasonably described by the simulations over a wide range of soil moisture conditions.

We used the transition time from continuous evaporation rates to decreasing evaporation rates to evaluate spatial variances in water content and water flow velocities for the tested soil macrostructures. After 1.75 days of evaporation, the simulations showed that the water content of the uppermost cm of the grassland soil was <0.2 cm^3 cm^{-3} (Figure 3c), while the lower sample part (2- to 5-cm depth) was still moist at 0.2–0.4 cm^3 cm^{-3}. A macropore, displayed in the upper left part of the sample, which had a large surface area, dried out faster than the average soil surface, which affected the surrounding domain nodes. While the water content gradually increased with depth, the heterogeneity of the soil structure influenced the water flux velocities over the entire sample height. To support the atmospheric demand given by the imposed gravimetric water loss at the boundary, both air-filled macropores and differences in water content caused some variation in the total water flow velocity of 0.23 cm day^{-1}. Throughout the water-filled soil matrix, water flowed in the direction of the evaporating soil surface, as indicated by the vector field of flow velocities.

For the ploughed soil, the water content of the uppermost soil clods was below 0.25 cm^3 cm^{-3} when evaporation rate started to decrease significantly (Figure 4c). Please note that the atmospheric demand was much lower during the evaporation experiment compared to the grassland soil. Below the first cm, water content was between 0.30 and 0.35 cm^3 cm^{-3}, which was close to the initial condition. The rough soil surface and the coarse macrostructure of the soil clods caused a wide distribution of water flux velocities from 0.01 to 0.40 cm day^{-1} with two histogram peaks, one at 0.09 cm day^{-1} and the other at 0.13 cm day^{-1} (Figure 4a). The highest fluxes, that is, >0.3 cm day^{-1}, were observed in the area just below the soil surface (Figure 4b). Here, the soil clods were connected by a few contact points (Figure 1a), and water had to be transported through these macro-bottlenecks to meet the atmospheric demand. The spatial heterogeneity in water flow was mainly localized in the uppermost 2.5 cm, as indicated by the vector field of flow velocities, which are not all directed toward the evaporating soil surface.

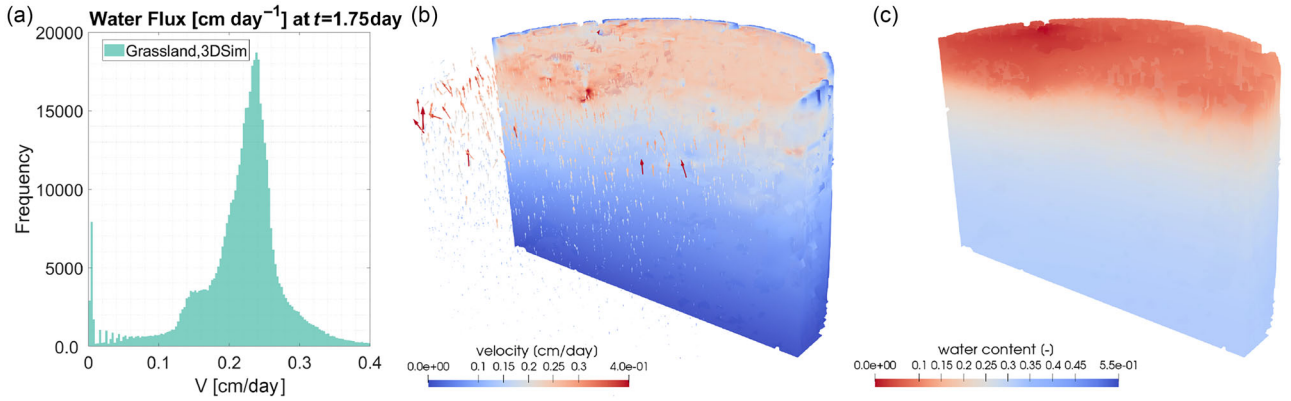

FIGURE 3 Simulated results of velocities of water flux (a, b) and water content (c) for the grassland soil sample at the point in time when evaporation rates were decreasing (time = 1.75 days). Results are displayed as a frequency distribution (a) and the spatial distribution calculated for every node (b). Arrows show the flow direction of soil water and are scaled according to the vector velocity. (c) The spatial distribution of water contents for the same simulation point in time.

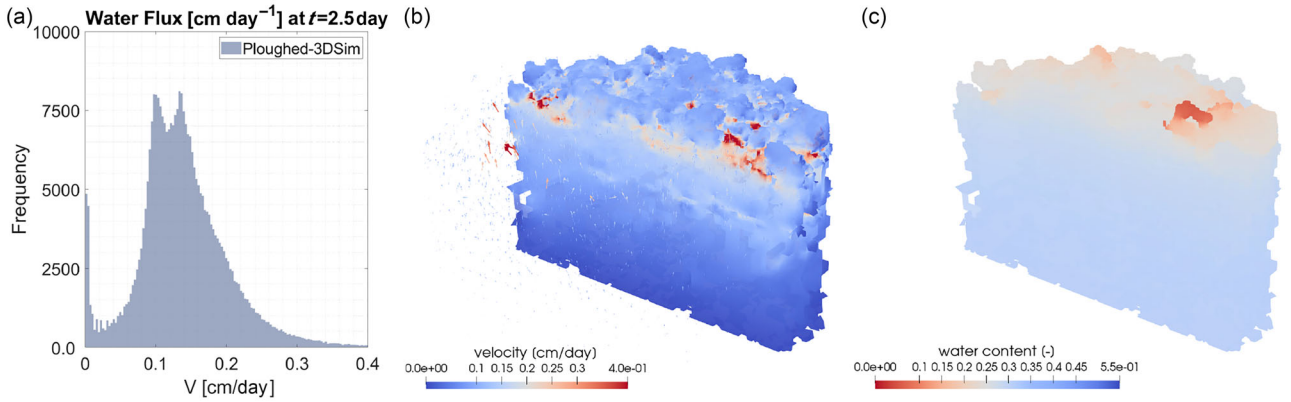

FIGURE 4 Simulated results of velocities of water flux (a, b) and water content (c) for in the ploughed soil sample at the point in time when evaporation rates were decreasing (time = 2.5 days). Results are displayed as a frequency distribution (a) and the spatial distribution calculated for every node (b). Arrows show the flow direction of soil water and are scaled according to the vector velocity. (c) shows the spatial distribution of water contents for the same simulation point in time.

4 | DISCUSSION

In this technical note, we present a methodology to conduct 3D simulations of general geometry with HYDRUS Suite for real soil systems based on X-ray μCT images. The method allows to characterize the effect of soil macrostructure on bare soil evaporation and potentially for any unsaturated transient water flow problem. The method is limited to the number of numerical nodes that can be used in HYDRUS, due to computer memory capacity as well as our fixed grid approach. In the current work, we had to first create a fixed regular (only changes with depth) numerical mesh and then assign material properties (soil–air) for each numerical element. The "air" elements were later deleted. Work should be done toward importing general geometries into HYDRUS and then generating a variable numerical mesh with high discretization near complex geometrical volumes (e.g., stones and aggregates of any arbitrary shape) and coarser discretization for simpler geometries (adaptive mesh). In that way, we will be able to utilize less numerical nodes and elements and, at the same time, preserve all the geometrical information, especially near the soil surface, if adaptive elements of <0.05 cm can be used. In the current method and mostly for the ploughed soil columns, some isolated elements near the soil surface remained after deleting the "air" elements, which had to be manually removed because they gave rise to numerical problems. We also note that this method allows only the quantification of relatively large-scale structural effects (macrostructure), mainly due to the memory limitations and the downscale of the images. A holistic investigation of the effect of soil structure (macro- and micro-pore) on bare soil evaporation requires at least the use of different local SHPs for each numerical node, following information from high-resolution images (e.g., multi-phase image segmentation like particulate

organic matter and stones). This could be included by using a multiphase image segmentation protocol rather than a binary segmentation (soil and air-filled pores) as used in this study. Alternatively, pore-scale simulations with the Navier–Stokes equations can be used, however, for smaller soil systems.

This technical note is based on two evaporation experiments with contrasting soil macrostructures, and we showed that the 3D image-based simulations were capable to describe the measured water losses and water potentials in two depths. Differences in the initial conditions, such as total water content or the SHP, were sensitive parameters, which may have caused the differences between measured and simulated tensions in the lower part of the sample. For both experiments, the divergence started when the soil surface dried much faster than the lower part of the soil core, thus the unsaturated hydraulic conductivity was significantly decreased. This also indicates the limitations of the wind method, which produced average hydraulic properties for non-linear conditions.

The simulations demonstrate that the loose soil macrostructure of the ploughed soil produced high heterogeneities in water flux velocities and water contents compared to the continuously connected soil matrix of the grassland soil. This can be explained by the rough surface and low number of hydraulically connected contact points between the clods, a phenomenon that has also been observed at field scale (Daigh & DeJong-Hughes 2017). However, it was also shown in grassland that air-filled biopores influenced the flow velocities within the sample and led to spatial heterogeneities in water content at the soil surface. As both soil macrostructure connectivity and water content are important determinants of water flow, these constraints become particularly important when soils dry out (Richard & Cellier, 1998; Sillon et al., 2003). These physical constraints for water flow, which have also been observed in field studies (Unkovich et al., 2018), offer the possibility that the method can be used for identifying optimum soil macrostructures that have a maximized effect on preserving water in modern agriculture fields or evaluating effects at larger spatial scales and more realistic boundary conditions (e.g., time series and groundwater interactions).

The focus of this work was to provide a workflow for including soil macrostructure and macro-connectivity effects of different land uses to study bare soil evaporation dynamics. Processes like albedo, soil surface roughness and resistance (Blöcher et al., 2023), local SHPS differences due to pore scale changes (Prat, 2007), and organic matter content and distribution (Minasny & McBratney, 2018) were not included in our model setup. All of these are expected to affect bare soil evaporation. Future work will be focused on those areas, as well as investigate the effect of the image resolution on the simulation results and finally compare simulations results with experimental observations.

5 | CONCLUSION

Soil macrostructure is an important characteristic of soils, which affects multiple soil functions, including soil water evaporation dynamics. The combination of HYDRUS 3D modeling of transient water flow for real soil structures quantified by X-ray µCT imaging enables a detailed analysis and visualization of the water flow regime within soil samples and identifying the effect of soil structure on the evaporation process. Even though numerical limitations required a rescaling of the structure, the method was sensitive to capture small structural heterogeneities, such as biopores or contact points between soil clods, and how they affect water content distribution and water fluxes within samples. Future work will be focused on extending this method to account for better representation of macro- and micro-soil structure as well as on simulating transient heat flow and solute transport in real soil systems.

AUTHOR CONTRIBUTIONS

Frederic Leuther: Conceptualization; investigation; methodology; visualization; writing—original draft. **Efstathios Diamantopoulos**: Conceptualization; investigation; methodology; visualization; writing—original draft.

ACKNOWLEDGMENTS

We would like to thank Dr. Miroslav Sejna for supporting us in importing the 3D structures into HYDRUS. The description of soil hydraulic properties and simulations of soil water dynamics with HYDRUS 3D used in this study are based on the fundamental contributions made by Rien van Genuchten to the field of soil physics and beyond.

CONFLICT OF INTEREST STATEMENT

The authors declare no conflicts of interest.

ORCID

Frederic Leuther https://orcid.org/0000-0001-6955-7892
Efstathios Diamantopoulos https://orcid.org/0000-0001-7870-0291

REFERENCES

Allen, R. G. (1998). *Crop evapotranspiration-guidelines for computing crop water requirements* (Irrigation and Drainage Paper no. 56). FAO.

Bittelli, M., Ventura, F., Campbell, G. S., Snyder, R. L., Gallegati, F., & Pisa, P. R. (2008). Coupling of heat, water vapor, and liquid water fluxes to compute evaporation in bare soils. *Journal of Hydrology*, *362*(3), 191–205. https://doi.org/10.1016/j.jhydrol.2008.08.014

Blöcher, J. R., Diamantopoulos, E., Durner, W., & Iden, S. C. (2023). Validating coupled flow theory for bare-soil evaporation under different boundary conditions. *Vadose Zone Journal*, *22*(6), e20277. https://doi.org/10.1002/vzj220339.20277

Brutsaert, W., & Chen, D. (1995). Desorption and the two stages of drying of natural tallgrass prairie. *Water Resources Research*, *31*(5), 1305–1313. https://doi.org/10.1029/95WR00323

Buades, A., Coll, B., & Morel, J. M. (2011). Non-local means denoising. *Image Processing On Line*, *1*, 208–212. https://doi.org/10.5201/ipol.2011.bcm_nlm

Daigh, A. L. M., & Dejong-Hughes, J. (2017). Fluffy soil syndrome: When tilled soil does not settle. *Journal of Soil and Water Conservation*, *72*(1), 10A–14A.

Daraghmeh, O. A., Jensen, J. R., & Petersen, C. T. (2009). Soil structure stability under conventional and reduced tillage in a sandy loam. *Geoderma*, *150*(1), 64–71. https://doi.org/10.1016/j.geoderma.2009.01.007

Geistlinger, H., & Leuther, F. (2018). Evaporation study for real soils based on HYPROP hydraulic functions and micro-CT-measured pore-size distribution. *Vadose Zone Journal*, *17*(1), 180041. https://doi.org/10.2136/vzj2018.02.0041

Hansen, C. D., & Johnson, C. R. (2005). *The visualization handbook*. Elsevier/Butterworth-Heinemann.

Iden, S. C., Blöcher, J. R., Diamantopoulos, E., & Durner, W. (2021). Capillary, film, and vapor flow in transient bare soil evaporation (1): Identifiability analysis of hydraulic conductivity in the medium to dry moisture range. *Water Resources Research*, *57*(5), e2020WR028513. https://doi.org/10.1029/2020WR028513

Iden, S. C., Diamantopoulos, E., & Durner, W. (2021). Capillary, film, and vapor flow in transient bare soil evaporation (2): Experimental identification of hydraulic conductivity in the medium to dry moisture range. *Water Resources Research*, *57*(5), e2020WR028514. https://doi.org/10.1029/2020WR028514

Jäger, H. J., Schmidt, S. W., Kammann, C., Grünhage, L., Müller, C., & Hanewald, K. (2003). The University of Giessen free-air carbon dioxide enrichment study: Description of the experimental site and of a new enrichment system. *Journal of Applied Botany*, *77*(5), 117–127.

Jawahar, C. V., Biswas, P. K., & Ray, A. K. (1997). Investigations on fuzzy thresholding based on fuzzy clustering. *Pattern Recognition*, *30*(10), 1605–1613.

Legland, D., Arganda-Carreras, I., & Andrey, P. (2016). MorphoLibJ: Integrated library and plugins for mathematical morphology with ImageJ. *Bioinformatics*, *32*(22), 3532–3534. https://doi.org/10.1093/bioinformatics/btw413

Leuther, F., & Schlüter, S. (2021). Impact of freeze—Thaw cycles on soil structure and soil hydraulic properties. *Soilless*, *7*(1), 179–191. https://doi.org/10.5194/soil-7-179-2021

Milly, P. C. D. (1984). A simulation analysis of thermal effects on evaporation from soil. *Water Research*, *20*(8), 1087–1098. https://doi.org/10.1029/WR020i008p01087

Minasny, B., & Mcbratney, A. B. (2018). Limited effect of organic matter on soil available water capacity. *European Journal of Soil Science*, *69*(1), 39–47.

Nassar, I. N., & Horton, R. (1997). Heat, water, and solution transfer in unsaturated porous media: I—Theory development and transport coefficient evaluation. *Transport in Porous Media*, *27*(1), 17–38. https://doi.org/10.1023/A:1006583918576

Or, D., Lehmann, P., Shahraeeni, E., & Shokri, N. (2013). Advances in soil evaporation physics—A review. *Vadose Zone Journal*, *12*(4), vzj2012.0163. https://doi.org/10.2136/vzj2012.0163

Peters, A. (2013). Simple consistent models for water retention and hydraulic conductivity in the complete moisture range. *Water Resources Research*, *49*(10), 6765–6780. https://doi.org/10.1002/wrcr.20548

Philip, J. R., & De Vries, D. A. (1957). Moisture movement in porous materials under temperature gradients. *Eos, Transactions American Geophysical Union*, *38*(2), 222–232. https://doi.org/10.1029/TR038i002p00222

Prat, M. (2007). On the influence of pore shape, contact angle and film flows on drying of capillary porous media. *International Journal of Heat and Mass Transfer*, *50*(7), 1455–1468. https://doi.org/10.1016/j.ijheatmasstransfer.2006.09.001

Prat, M. (2011). Pore network models of drying, contact angle, and film flows. *Chemical Engineering & Technology*, *34*(7), 1029–1038. https://doi.org/10.1002/ceat.201100056

Richard, G., & Cellier, P. (1998). Effect of tillage on bare soil energy balance and thermal regime: An experimental study. *Agronomie*, *18*(3), 163–181.

Sakai, M., Jones, S. B., & Tuller, M. (2011). Numerical evaluation of subsurface soil water evaporation derived from sensible heat balance. *Water Resources Research*, *47*(2), W02547. https://doi.org/10.1029/2010WR009866

Schindelin, J., Arganda-Carreras, I., Frise, E., Kaynig, V., Longair, M., Pietzsch, T., Preibisch, S., Rueden, C., Saalfeld, S., Schmid, B., Tinevez, J.-Y., White, D. J., Hartenstein, V., Eliceiri, K., Tomancak, P., & Cardona, A. (2012). Fiji: An open-source platform for biological-image analysis. *Nature Methods*, *9*(7), 676–682. https://doi.org/10.1038/nmeth.2019

Schindler, U. (1980). Ein schnellverfahren zur messung der wasserleitfähigkeit im teilgesättigten boden an stechzylinderproben. *Archiv für Acker- und Pflanzenbau und Bodenkunde*, *24*(1), 1–7.

Schlüter, S., Leuther, F., Vogler, S., & Vogel, H.-J. (2016). X-ray microtomography analysis of soil structure deformation caused by centrifugation. *Solid Earth*, *7*(1), 129–140. https://doi.org/10.5194/se-7-129-2016

Sillon, J. F., Richard, G., & Cousin, I. (2003). Tillage and traffic effects on soil hydraulic properties and evaporation. *Geoderma*, *116*(1), 29–46. https://doi.org/10.1016/S0016-7061(03)00092-2

Šimůnek, J., Šejna, M., & Van Genuchten, M. Th. (2018). New features of version 3 of the HYDRUS (2D/3D) computer software package. *Journal of Hydrology and Hydromechanics*, *66*(2), 133–142. https://doi.org/10.1515/johh-2017-0050

Unkovich, M., Baldock, J., & Farquharson, R. (2018). Field measurements of bare soil evaporation and crop transpiration, and transpiration efficiency, for rainfed grain crops in Australia—A review. *Agricultural Water Management*, *205*, 72–80. https://doi.org/10.1016/j.agwat.2018.04.016

Vanderborght, J., Fetzer, T., Mosthaf, K., Smits, K. M., & Helmig, R. (2017). Heat and water transport in soils and across the soil-atmosphere interface: 1. Theory and different model concepts. *Water Resources Research*, *53*(2), 1057–1079. https://doi.org/10.1002/2016WR019982

Weber, T. K. D., Iden, S. C., & Durner, W. (2017). Unsaturated hydraulic properties of *Sphagnum* moss and peat reveal trimodal pore-size distributions. *Water Resources Research*, *53*(1), 415–434. https://doi.org/10.1002/2016WR019707

SUPPORTING INFORMATION

Additional supporting information can be found online in the Supporting Information section at the end of this article.

How to cite this article: Leuther, F., & Diamantopoulos, E. (2024). Simulating bare soil evaporation for undisturbed soil cores—Using HYDRUS 3D simulation on X-ray μCT determined soil macrostructures. *Vadose Zone Journal*, *23*, e20339. https://doi.org/10.1002/vzj2.20339